Journal of Materials Chemistry C

ROYAL SOCIETY OF CHEMISTRY

PAPER

View Article Online
View Journal | View Issue

Cite this: J. Mater. Chem. C, 2020, 8, 4810

Huge enhancement of Sm^{2+} emission *via* Eu^{2+} energy transfer in a SrB_4O_7 pressure sensor†

Teng Zheng, [a] Marcin Runowski, *[a] Przemysław Woźny, [a] Stefan Lis [a] and Víctor Lavín [b]

Received 27th January 2020,
Accepted 29th February 2020

DOI: 10.1039/d0tc00463d

rsc.li/materials-c

Taking advantage of the excellent pressure-sensing properties of the Sm^{2+} ion in the SrB_4O_7 crystal, we demonstrate an enormous enhancement of about 60 times in the emission intensity of Sm^{2+} ions when Eu^{2+} ions are also incorporated into the crystalline structure. This enhancement is induced by the energy transfer from Eu^{2+} to Sm^{2+} ions. The spectral position of the ultra-narrow and most intense $^5D_0 \rightarrow {}^7F_0$ emission line in the material was correlated with pressure and successfully calibrated up to about 58 GPa. The material exhibits favorable pressure-sensing features, *i.e.* $d\lambda/dp \approx 0.29$ nm GPa^{-1}, negligible temperature-dependent shift, narrow and well-separated emission lines, and a strong luminescence signal. The samples also exhibit multicolor tunable luminescence from orange-red to amaranth, and to warm-white light, depending on the excitation wavelength used and dopant content in the matrix, allowing their potential application in white light emitting diode (LED) devices.

Introduction

Pressure shapes stars and planets, continents and oceans, and affects all aspects of our lives.[1] Pressure also has a crucial influence on the physicochemical properties of materials. Compression of materials under high-pressure conditions has been widely utilized for the study of pressure-induced changes of physicochemical characteristics of substances, formations of new phases or materials under extreme conditions, spectroscopic and structural variation of the chemical compounds, *etc.*[2–10] When trying to mimic these processes for scientific and industrial purposes in the laboratory using a high pressure anvil cell, a quick and precise determination of pressure is of paramount importance and, thanks to the transparency of diamonds and other gems in the visible range, optical pressure calibrants are often used.[11]

In the case of a static high pressure experiment, the combination of a sample with a variety of hydrostatic pressure transmitting media (PTM) is a typical assemblage for diamond anvil cell (DAC) system, using the calibration of the line shift of the fluorescence at around 694 nm of Cr^{3+} ion in ruby, *i.e.* $d\lambda/dp \approx 0.35$ nm GPa^{-1}, for the pressure determination.[12–15] However, due to the pressure-induced solidification of most of the commonly used PTMs and the subsequent loss of hydrostaticity in the sample's chamber,[15–18] a large error occurs in the ruby spectral data analysis that significantly reduces the accuracy of the pressure determination under very high pressure conditions. This is because of the relatively broad ($\approx$0.8 nm at ambient condition) emission bands of ruby and the strong overlapping of the ruby peaks (R_1 and R_2) under non-hydrostatic, high-pressure conditions. Moreover, the fluorescence line shift of ruby is strongly temperature-dependent, *i.e.* $d\lambda/dT \approx 0.007$ nm K^{-1}, which limits its pressure-sensing capability to the low-temperature range.

The SrB_4O_7:Sm^{2+} compound has been reported in many works as a splendid alternative to ruby as pressure gauge,[18–21] thanks to its favorable features such as: (I) an isolated, narrow ($\approx$0.2 nm) and intense $^5D_0 \rightarrow {}^7F_0$ emission band (0–0 line) located at around 685 nm; (II) a large pressure-induced shift of the 0–0 line ($\approx$0.25 nm GPa^{-1}), comparable to that of Cr^{3+} in ruby, (III) a negligible temperature coefficient (10^{-4} nm K^{-1}), and (IV) excellent thermal, chemical and structural stabilities. However, despite these benefits, and as it also happens to ruby, the inevitable decrease of Sm^{2+} luminescence intensity under pressure may limit the measurable pressure range and also may diminish the sensing accuracy.

The divalent lanthanide (Ln) ions are interesting luminescent centers because of the smaller energy gap between the $4f^n$ ground and the first excited $4f^{n-1}5d$ configurations compared to the Ln^{3+} ions.[22–29] This smaller energy difference increases the mixing of wavefunctions of the different configurations, *i.e.* increasing the 5d state opposite parity character of the 4f wavefunctions,

[a] Adam Mickiewicz University, Faculty of Chemistry, Uniwersytetu Poznańskiego 8, 61-614 Poznań, Poland. E-mail: runowski@amu.edu.pl; Tel: +48618291778
[b] Departamento de Física, MALTA Consolider Team and IUdEA, Universidad de La Laguna, Apdo. Correos 456, E-38200 San Cristóbal de La Laguna, Santa Cruz de Tenerife, Spain

† Electronic supplementary information (ESI) available: Experimental details; XRD data; SEM images; EDX mapping and spectra; emission spectra; FWHM in pressure; temperature shift; luminescence decay curves and luminescence lifetime; CIE diagram. See DOI: 10.1039/d0tc00463d

that shorten the lifetime and increases the intensity of the luminescence of Ln^{2+} ions.[30] The divalent europium ion (Eu^{2+}) has many advantages, such as intense broad excitation and emission bands corresponding to the allowed $4f^65d \leftrightarrow 4f^7$ transitions, relatively low reduction potential, relatively high stability, *etc.*[31–35] Thanks to the large absorption in the UV region of Eu^{2+} in many host materials, this ion may exhibit excellent sensitization effects to other lanthanide ions.[36–40] According to energy transfer (ET) mechanism,[41–43] such a process occurring from sensitizer (Eu^{2+}) to activator ions can effectively enhance emission of the luminophore. A host material based on the SrB_4O_7 crystal structure is a good choice for effective combination of sensitizing properties of Eu^{2+} ions with the targeted Sm^{2+} activator ions, to enhance luminescence performance of the system. This is because SrB_4O_7 host reveals excellent stabilization of both Eu^{2+} and Sm^{2+}, even at high temperature in an oxidizing atmosphere. Moreover, the similar ionic radii of the dopant and host ions ($R_{Eu^{2+}}$ = 1.39 Å, $R_{Sm^{2+}}$ = 1.41 Å and $R_{Sr^{2+}}$ = 1.40 Å) provide less lattice distortion of the synthesized crystals.[44–47]

Many works have focused on the synthesis of different compounds doped with Sm^{2+} and other trivalent lanthanide ions, *i.e.* Ce^{3+}, Er^{3+}, Tm^{3+}, *etc.*, and their use for pressure sensing applications.[25,26,48–53] However, there are no reports concerning signal enhancement of pressure sensors *via* the ET processes from Eu^{2+} to other $Ln^{2+/3+}$ ions, which may significantly increase the emission intensity of various co-doped optical sensors, working under high pressure conditions. Herein, we report a huge enhancement of about 60 times in the emission intensity of Sm^{2+} caused by the $Eu^{2+} \rightarrow Sm^{2+}$ ET in the co-doped SrB_4O_7 compound synthesized by a simple solid-state method in air, and its application as a well-calibrated and accurate optical pressure sensor, which can work simultaneously under extreme conditions of pressure and temperature. In addition, we also demonstrate multi-color tunable emission from orange-red to warm white, depending on the concentration of Sm^{2+} and Eu^{2+} ions in the host and the excitation wavelength used.

Results and discussions

Structural and morphological properties

Information concerning the raw material used, synthesis and characterization are available in the ESI.† The powder X-ray diffraction (XRD) patterns (Fig. S1 in ESI†) of the SrB_4O_7:0.01Sm^{2+},*x*Eu^{2+} (*x* = 0, 0.005, 0.01, 0.03, 0.05, 0.07 and 0.09) micro-particles fit well with the reference patterns (card no. 071-2191) from the ICDD standards database: orthorhombic SrB_4O_7 phase with space group $Pmn2_1$. The graphical representation of crystal structure is shown in Fig. 1a, where it is indicated that only one Sr^{2+} site exists in the structure of SrB_4O_7 host occupying a nonahedron (coordination number: 9) with local

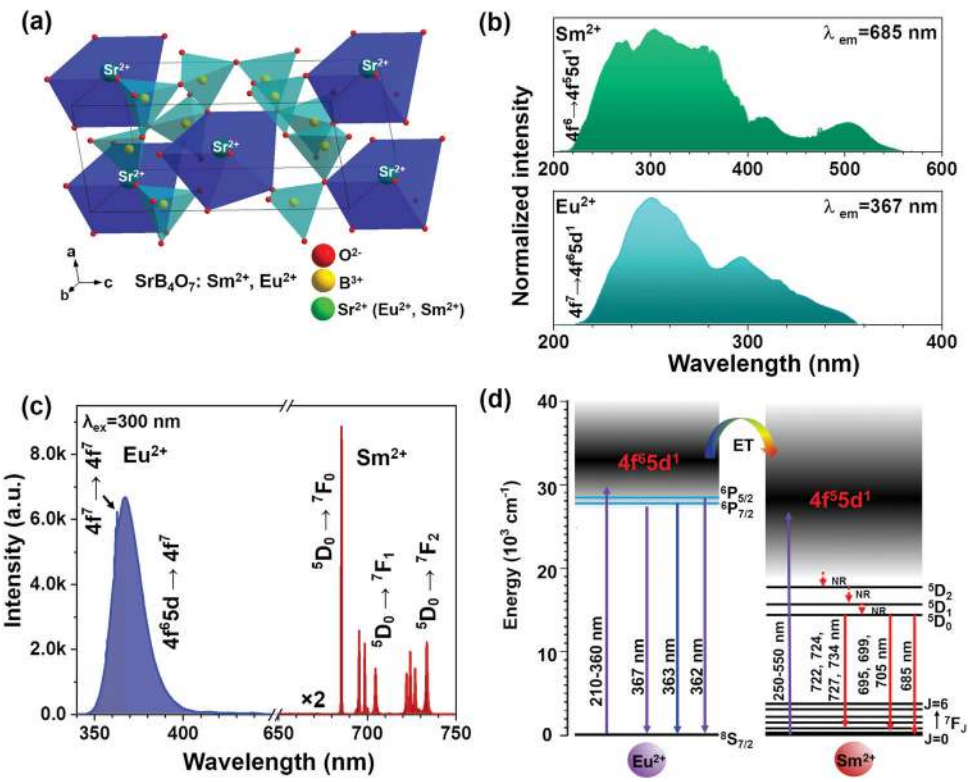

Fig. 1 (a) Graphical representation of the crystal structure of orthorhombic SrB_4O_7 matrix ($Pmn2_1$ space group). (b) The excitation spectra monitoring the emission at 685 nm for Sm^{2+} (top) and λ_{em} = 367 nm for Eu^{2+} (bottom) and (c) the emission spectrum at λ_{ex} = 300 nm of the SrB_4O_7:0.01Sm^{2+},0.03Eu^{2+} compound. (d) Simplified energy level diagram for the Sm^{2+} and Eu^{2+} ions and emission processes in the co-doped SrB_4O_7 system with the possible $Eu^{2+} \rightarrow Sm^{2+}$ ET process.

point symmetry C_{2v}, and the cell parameters are: a = 4.431(4) Å, b = 10.707(10) Å, c = 4.237(4) Å, V = 200.810 Å^3.

The morphology of the synthesized products was inspected by a scanning electron microscopy (SEM), and the representative SEM images of SrB_4O_7:0.01Sm^{2+},xEu^{2+} samples (x = 0, 0.01, 0.03, 0.05) are shown in Fig. S2 (ESI†). The synthesized products are composed of irregular, nearly-spherical micro-particles (typical of inorganic borates), whose sizes range from approximately ~0.2 to 2.0 μm. With increasing content of Eu^{2+}, from 0 to 5 mol% (x = 0–0.05), the particle sizes vary slightly, which can be attributed to the similar ionic radii between the host and dopant ions.[54–56] In Fig. S2e–k (ESI†), the representative elemental mapping results and the EDX spectrum of the SrB_4O_7:0.01Sm^{2+},0.03Eu^{2+} compound revealed that the obtained phosphor consist of Sr, B, O, Eu and Sm, and these elements are uniformly distributed in the prepared product over the whole particle volume.

Optical properties at ambient conditions

The photoluminescence (PL) emission and excitation spectra, as well as luminescence decay curves, of the samples obtained were recorded under the same experimental conditions, and were corrected for the apparatus response. In Fig. 1b, the excitation spectra are given for the SrB_4O_7:0.01Sm^{2+},0.03Eu^{2+} compound recorded monitoring the emission at 685 nm for Sm^{2+} (top) and 367 nm for Eu^{2+} (bottom). It was found that the excitation spectra of both Sm^{2+} and Eu^{2+} consist of two overlapped broad peaks with maxima at around ≈250 nm and ≈300 nm, which are due to the splitting of 5d orbital into the t_{2g} and e_g components.[57] Upon UV light excitation at 300 nm (the highest peak in excitation spectra of Sm^{2+} in Fig. 1b), the PL emission spectrum of the SrB_4O_7:0.01Sm^{2+},0.03Eu^{2+} compound was examined. As shown in Fig. 1c, the emission spectrum consists of UV-violet and red bands. In the UV-violet region, the detected emission band can be deconvoluted into two peaks, *i.e.* the characteristic $4f^65d \rightarrow 4f^7$ transition of Eu^{2+} centered at 367 nm (broad band) and the rarely observed $4f^7$–$4f^7$ line-type (narrow) transitions of Eu^{2+} centered at ≈362.1 and ≈362.7 nm.[58–61] On the other hand, the red emissions of Sm^{2+}, located in the range of ≈680–750 nm, correspond to $^5D_0 \rightarrow {}^7F_0$ (685.4 nm), $^5D_0 \rightarrow {}^7F_1$ (695.4, 698.6, 704.6 nm), $^5D_0 \rightarrow {}^7F_2$ (722.1, 724.2, 727.0 and 733.5 nm) and they are associated with $4f^6$–$4f^6$ intra-configurational transitions of Sm^{2+} ions. It is clearly seen that the $^5D_0 \rightarrow {}^7F_0$ transition of Sm^{2+} exhibits its characteristic isolated, narrow and intense singlet band located at 685.4 nm. In the case of inevitable broadening of emission peaks under high pressure conditions, such a characteristic intensive, singlet and narrow 0–0 line of Sm^{2+} in a co-doped SrB_4O_7, reveals its superiority for high-pressure measurements, in comparison with the emissions bands of other transition metal ions (*e.g.* Mn^{4+}, Ce^{3+}, Er^{3+}).[53,62–64] This is attributed to the fact that the lowest emitting level and the ground state of the Sm^{2+} ion are singlets, *i.e.* non-degenerated multiplets with a total angular quantum momentum (J number) equal to zero. In addition, the $^5D_0 \rightarrow {}^7F_1$ band presents three sharp peaks, while the $^5D_0 \rightarrow {}^7F_2$ band presents only four out of five peaks. Hence, all the observed Sm^{2+} bands are split in a maximum of $2J + 1$ Stark components, which further confirms only one Sm^{2+} local symmetry site (local point symmetry C_{2v}) existing in the SrB_4O_7 structure.

To better comprehend the feasible ET process and the luminescence mechanisms governing the generation of UV-violet and red emissions, the simplified energy level diagram of Eu^{2+} and Sm^{2+} ions is illustrated in Fig. 1d. With the excitation of UV light (from 210 to 360 nm), the Eu^{2+} ions can be excited from their ground $^8S_{7/2}$ level to the excited $4f^65d^1$, as well as $^6P_{5/2}$ and $^6P_{7/2}$ levels, and then radiatively relax to the ground state, accompanied with a broad UV-violet emission ($5d \rightarrow 4f$) overlapping with line-type emission ($4f^7 \rightarrow 4f^7$) of Eu^{2+}. Meanwhile, the Sm^{2+} ions populating the $^7F_0$ ground state can be excited to the $4f^55d^1$ first excited configuration of Sm^{2+} when pumping at λ_{ex} = 250–550 nm. Afterward, non-radiative (NR) decays occur, populating the lowest excited level $^5D_0$, finally leading to a series of radiative $^5D_0 \rightarrow {}^7F_J$ transitions, giving rise to the characteristic narrow bands of the red emission of Sm^{2+} ions. We assume that there is an energy transfer (ET) process between the Eu^{2+} and Sm^{2+} ions in the SrB_4O_7 host, which will be discussed in detail in the following paragraphs.

In order to explore the influence of Eu^{2+} ion concentration on the emission properties of the synthesized samples, the emission

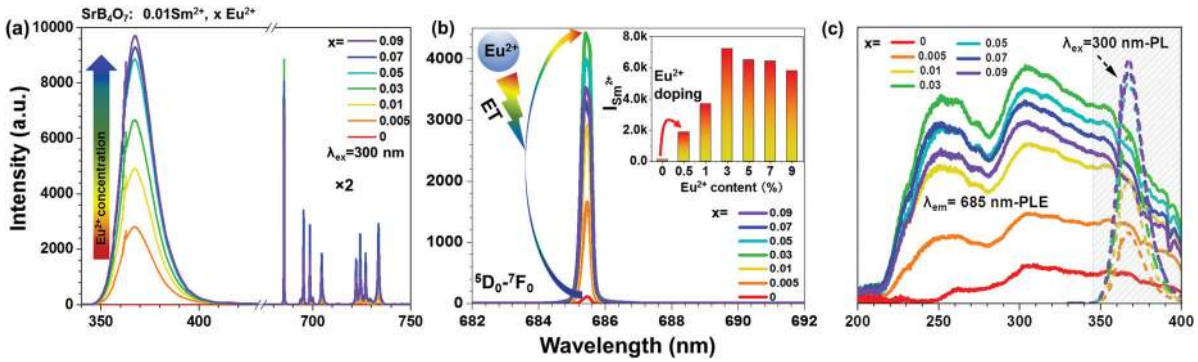

Fig. 2 (a) Emission spectra of the SrB_4O_7:0.01Sm^{2+},xEu^{2+} (x = 0, 0.005, 0.01, 0.03, 0.05, 0.07 and 0.09) compounds, using λ_{ex} = 300 nm at ambient condition. (b) Magnified emission spectra showing the 0–0 line of Sm^{2+} as a function of Eu^{2+} content x. (c) Excitation spectra for Sm^{2+} ions monitoring the emission at 685 nm (solid lines) and their overlapping part (shaded area) with Eu^{2+} emission (dashed lines) of the samples.

spectra exciting at λ_{ex} = 300 nm of the samples as a function of the Eu^{2+} ion content are shown in Fig. 2a. It is clearly seen that all the emission spectra consist of UV-violet emission bands of Eu^{2+} ions and red emission lines from Sm^{2+} ions, except of the sample without Eu^{2+} ions (SrB_4O_7:0.01Sm^{2+}) that only shows Sm^{2+} emission lines. With increasing the Eu^{2+} ion content from 0.5 to 9 mol% (x = 0.05–0.9), the shape of emission peaks scarcely varies, whereas the emission intensity and the Eu^{2+}/Sm^{2+} band intensity ratios are greatly dependent on the Eu^{2+} doping content. In the UV-violet region, the emission intensity of Eu^{2+} maintains an upward tendency with increasing the Eu^{2+} doping content from 0 to 9 mol%. For detailed investigation of the sensitization effect of Eu^{2+} in the synthesized samples, the magnified emission spectra of the Sm^{2+}: 0–0 line (in a narrow range) as a function of the Eu^{2+} doping content are shown in Fig. 2b. As disclosed, the Sm^{2+} emission intensity of the samples is highly dependent on the Eu^{2+} concentration and the best enhancement occurs for x = 0.03 (inset in Fig. 2b). Based on the integrated emission intensity of Sm^{2+} in the SrB_4O_7:0.01Sm^{2+},$x$$Eu^{2+}$ samples (see Table S1 in ESI†), it is clearly seen that the addition of even 0.5 mol% of Eu^{2+} results in the ≈16-times enhancement in emission intensity of Sm^{2+} compared to the sample without Eu^{2+} ions. As the Eu^{2+} content further increases, the enhancement demonstrates an upward tendency, exhibiting its optimal value, *i.e.* about 60 times enhancement, with 3 mol% of Eu^{2+}. Afterwards, the emission intensity of Sm^{2+} ions starts to decrease when the doping concentration is over 3 mol%, probably due to the concentration quenching effects. Such a large increase in the intensity of Sm^{2+} emission in this material may be attributed to the ET phenomenon, occurring from Eu^{2+} to Sm^{2+} ions.

For the sake of studying the possible ET process from the Eu^{2+}–Sm^{2+} ions, the emission spectra recorded at λ_{ex} = 300 nm (Eu^{2+}) and the excitation spectra at λ_{em} = 685 (Sm^{2+}) of SrB_4O_7:0.01Sm^{2+},$x$$Eu^{2+}$ (x = 0–0.09) are shown in Fig. 2c, emphasizing their overlapping parts. It can be clearly seen that all the obtained samples have a very broad excitation band from 200 to over 400 nm, with the highest peak at around 300 nm, associated with Sm^{2+} ions that overlaps the Eu^{2+} emission band, located in the range from 345 to 400 nm. In fact, Eu^{2+} begins to emit even at lower wavelengths, however, due to the technical reasons, *i.e.* the necessity of using a long-pass (350 nm) filter, this emission is partially cutoff. The overlapping area indicates the resonant channel for ET from Eu^{2+} to Sm^{2+} ions, which occurs in the Sm^{2+}–Eu^{2+} co-doped SrB_4O_7 system, leading to the enhancement of Sm^{2+} emission.[65]

The Commission Internationale de l'Eclairage (CIE) chromaticity diagram for the SrB_4O_7:0.01Sm^{2+},$x$$Eu^{2+}$ (x = 0–0.09) samples and the corresponding photographs of the samples under irradiation with a 254 nm UV lamp are shown in Fig. 3a. All the samples obtained are white powders in daylight. The presented colors in the CIE diagram (based on the emission spectra characteristics) agree with the luminescence photographs. As disclosed, the samples obtained exhibit multi-color tunable emission from orange-red to warm white, depending on the Eu^{2+} content in

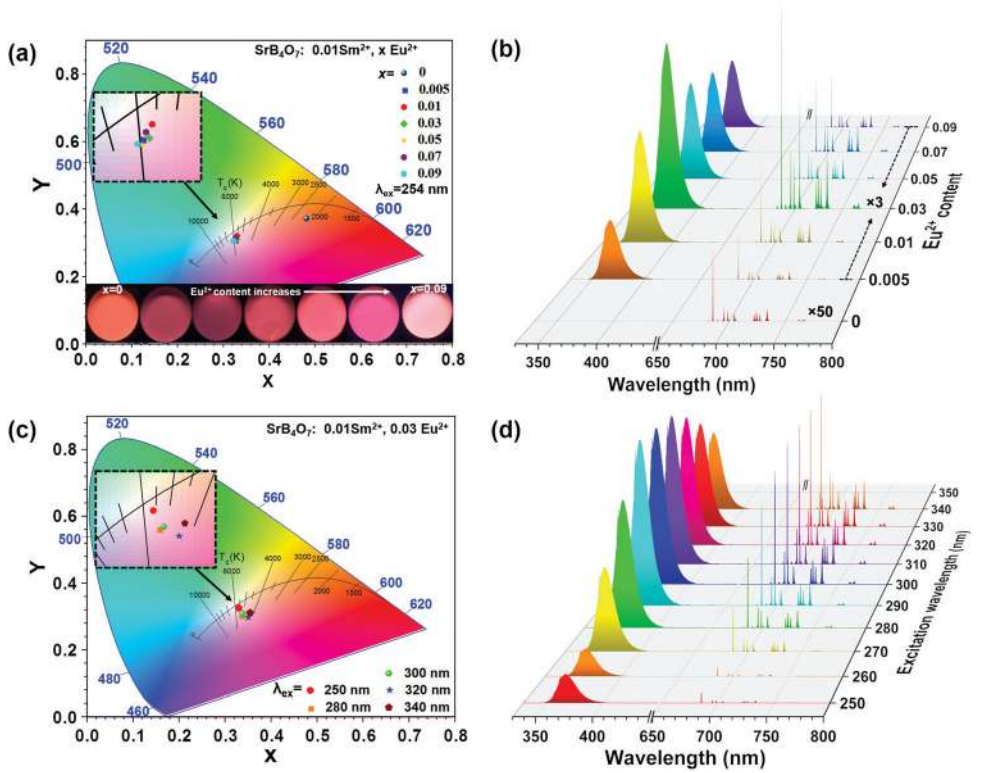

Fig. 3 (a) CIE chromaticity diagram and luminescence images of the SrB_4O_7:0.01Sm^{2+},$x$$Eu^{2+}$ (x = 0–0.09) phosphors, excited at 254 nm, and (b) the corresponding emission spectra. (c) CIE chromaticity diagram of SrB_4O_7:0.01Sm^{2+},0.03Eu^{2+} as a function of representative excitation wavelengths, and (d) the corresponding emission spectra.

the phosphor. The corresponding emission spectra excited at 254 nm are shown in Fig. 3b. Moreover, as shown in Fig. 3c and d, the emission color of the best-enhanced sample (SrB_4O_7:0.01Sm^{2+},0.03Eu^{2+}) can also be tuned depending on the excitation wavelength used. Noteworthy, the determined color coordinates of the Sm^{2+}–Eu^{2+} co-doped SrB_4O_7 are very close to the white illumination (0.310, 0.316), *e.g.* 0.322, 0.306 (9 mol% of Eu^{2+}) and 0.330, 0.325 (3 mol% of Eu^{2+}), indicating that the phosphors obtained have potential application in white LED. All determined color coordinates as a function of the Eu^{2+} doping concentration and the excitation wavelength used are shown in Tables S2 and S3 in ESI,† respectively.

Optical properties at high pressure

To investigate the pressure-sensing abilities of Sm^{2+} in the Eu^{2+} co-doped SrB_4O_7 material, the best-enhanced sample, *i.e.* SrB_4O_7:0.01Sm^{2+},0.03Eu^{2+}, was used in high-pressure measurements from ambient pressure up to about 58 GPa. The experimental setup used for the measurements of high-pressure luminescence is schematically presented in Fig. 4a. Due to technical reasons (availability of a high-power, focusable light source), the sample was excited at 280 nm, which is close to the optimal excitation wavelength. Technical details concerning measurements under high-pressure and sample preparation for DAC are presented in ESI.†

The normalized emission spectra of the SrB_4O_7:0.01Sm^{2+},0.03Eu^{2+} material under pressure are shown in Fig. 4b. It can be clearly seen that, when the pressure increases, the red-shifts of the $^5D_0 \rightarrow {}^7F_0$ and $^5D_0 \rightarrow {}^7F_1$ emission peaks are observed. These shifts to lower energies under pressure are caused by an overall contraction of the $4f^N$ ground configuration leading to a reduction in the energy difference between the ground state and the excited state of the $^{2S+1}L_J$ multiplets.[11,51] This phenomenon is related to decreasing coulomb and spin–orbit interactions under pressure, and it is called nephelauxetic effect,[66] which can be accounted by a reduction of the free-ion parameters due to the increasing covalent character of the lanthanide–oxygen bonds, when interatomic distances decrease along with decreasing volume. Superimposed on the reduction in multiplets splitting, there is an increase in the splitting of the multiplets, ascribed to an increase of the crystal field interaction between the 4f electron of the lanthanide ion and the valence electrons of the oxygen anions of the first coordination shell, when interatomic distances decrease with pressure.[10] This can be clearly observed in the splitting of the $^5D_0 \rightarrow {}^7F_1$ emission peaks that increases from ≈9.2 nm (≈188 cm^{-1}) at ambient pressure to ≈11.8 nm (≈230 cm^{-1}) at 58.07 GPa. The emission spectra for all recorded pressure values are shown in Fig. S3(a–c) (ESI†).

The calibration curve for the spectral position of the Sm^{2+} 0–0 line as a function of pressure, in the compression and decompression cycles is presented in Fig. 4c. The peak centroid reversibly shifts from about 685.4 nm at ambient pressure to 702.3 nm at 58.07 GPa, which can be well fitted (R^2 = 0.998) to a linear function. The calculated shift rate for this band is $d\lambda/dT \approx 0.29$ nm GPa^{-1}, which is close to the shifts of the SrB_4O_7:Sm^{2+} reported previously[18–21,45] and also to that

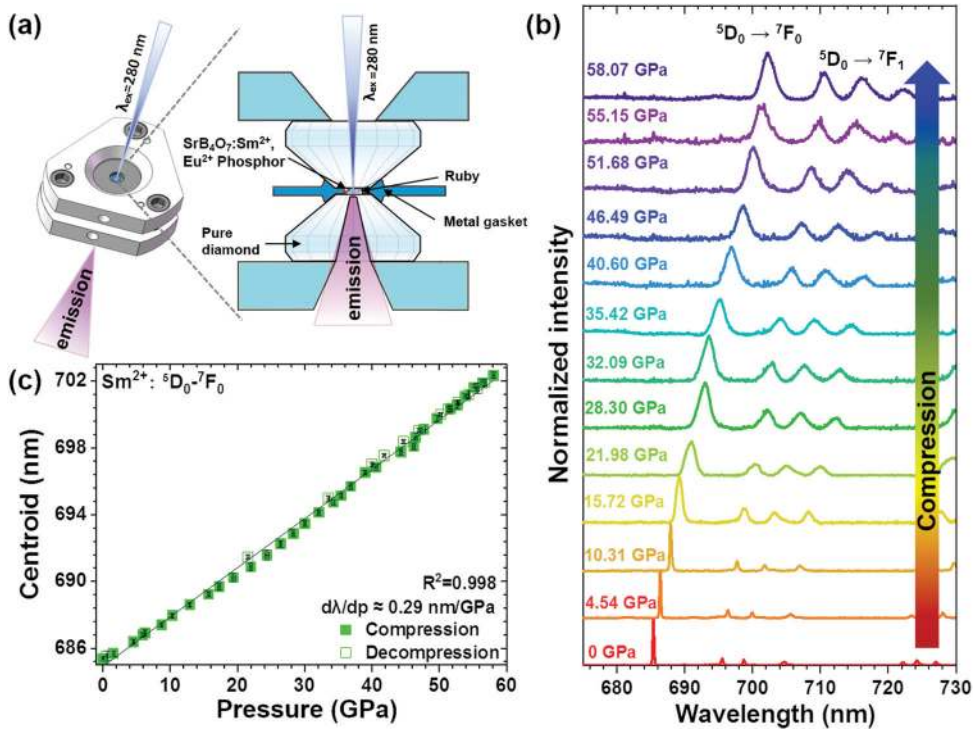

Fig. 4 (a) Schematic configuration of the setup used for high-pressure luminescence measurements. (b) The normalized emission spectra of the SrB_4O_7:0.01Sm^{2+},0.03Eu^{2+} material as a function of pressure; λ_{ex} = 280 nm. (c) Spectral positions (peak centroids) of the $^5D_0 \rightarrow {}^7F_0$ emission peak as a function of pressure. The filled symbols represent the compression and the empty ones decompression data.

Table 1 Determined decay times for the Eu^{2+} $4f^65d^1 \rightarrow 4f^7$ transition in the SrB_4O_7:ySm^{2+},0.05Eu^{2+} (y = 0.005, 0.01, 0.02, 0.03 and 0.05) compounds synthesized

Sample (% Sm^{2+})	Eu^{2+} ($4f^65d^1 \rightarrow 4f^7$)					
	τ_1 (μs)	A_1 (%)	τ_2 (μs)	A_2 (%)	τ (μs)	R^2
0.5	0.668 ± 0.006	0.117	2.616 ± 0.002	0.883	2.388	>0.999
1	0.570 ± 0.006	0.142	2.500 ± 0.004	0.858	2.226	>0.999
2	0.559 ± 0.002	0.189	2.326 ± 0.002	0.811	1.992	>0.999
3	0.461 ± 0.002	0.249	2.227 ± 0.002	0.751	1.787	>0.999
5	0.398 ± 0.002	0.272	2.117 ± 0.003	0.728	1.649	>0.999

reported for ruby.[12,15] All the exact $d\lambda/dP$ values, and the initial and final spectral positions of the peak centroids ($^5D_0 \rightarrow {}^7F_0$ and $^5D_0 \rightarrow {}^7F_1$ transitions) are presented in Table S4 in ESI.† The 0–0 line of Sm^{2+} in the SrB_4O_7:Eu^{2+}–Sm^{2+} material is almost temperature-independent showing a relatively low thermal-quenching effect of $d\lambda/dT \approx -2.8 \times 10^{-4}$ nm K^{-1}, as reported for SrB_4O_7:Sm^{2+} in several papers,[18–21,45] which we additionally confirmed for our compound (see Fig. S4 in ESI†). The low thermal-quenching effect presented, *i.e.* ≈75% of the initial emission intensity at 420 K (working temperature of LED devices), is beneficial not only for pressure sensing, but also for potential use in lighting applications.[67,68]

The broadening of the $^5D_0 \rightarrow {}^7F_0$ and $^5D_0 \rightarrow {}^7F_1$ band profiles together with the increase in pressure (volume reduction) is clearly seen in the presented emission spectra (Fig. 4b). At ambient conditions, the 0–0 line is extremely narrow, *i.e.* the full width at half maximum $\Gamma \approx 0.23$ nm. It keeps an upward tendency with increasing pressure (see Fig. S3d, ESI†) and increases to ≈1.81 nm at 26.42 GPa, which is mainly due to the increasing non-hydrostaticity of the pressure transmitting medium used. Then, this peak undertakes a slower broadening, up to ≈2.27 nm at 58.07 GPa, with an average $d\Gamma/dP \approx 14.5 \times 10^{-3}$ nm GPa^{-1}.

Confirmation of ET from Eu^{2+} to Sm^{2+} in co-doped SrB_4O_7

In order to fully confirm the ET from Eu^{2+} to Sm^{2+}, a series of SrB_4O_7 doped with a constant amount of Eu^{2+} and varied content of Sm^{2+} were synthesized. As shown in Fig. S5a (ESI†), the XRD patterns of the SrB_4O_7:ySm^{2+},0.05Eu^{2+} (y = 0.005, 0.01, 0.02, 0.03 and 0.05) micro-particles indicated that all phosphors were successfully synthesized. In Fig. S5b (ESI†), the emission spectra are shown for the excitation wavelength λ_{ex} = 254 nm, indicating a gradual increase in the Sm^{2+} emission intensity and a deterioration of Eu^{2+} emission, as the Sm^{2+} doping content increases. In the inset in Fig. S5(b) (ESI†), the integrated emission intensity ratio of Sm^{2+}/Eu^{2+} as a function of Sm^{2+} concentration shows an upward tendency. The CIE diagram for the synthesized phosphors at λ_{ex} = 254 nm, *i.e.* the comparison of the emission color between different doping content of Sm^{2+} is shown in Fig. S5c (ESI†). The colors presented in this CIE diagram agree with the luminescence photographs. The corresponding color coordinates are listed in Table S5 (ESI†). Accordingly, the corresponding emission color can be tuned from orange-red to amaranth depending on the Sm^{2+} content in the SrB_4O_7:ySm^{2+},0.05Eu^{2+} samples.

The photoluminescence decay curves of the as-prepared SrB_4O_7:ySm^{2+},0.05Eu^{2+} (y = 0.005–0.05) samples are presented in Fig. S5d (ESI†). The luminescence decay curves of these phosphors were recorded at λ_{em} = 367 nm for the Eu^{2+} ion after the excitation at 300 nm. The decay curves of Eu^{2+} emission show a non-exponential character (due to the high doping concentration). However, to analyze the tendency of luminescence lifetimes as a function of Sm^{2+} content, and confirm the $Eu^{2+} \rightarrow Sm^{2+}$ ET phenomenon, the decay profiles were fitted ($R^2 > 0.999$) to the bi-exponential function:

$$I = A_1 \exp(-x/\tau_1) + A_2 \exp(-x/\tau_2) \quad (1)$$

where I is the luminescence intensity at time x, A is the amplitude, and τ is the emission lifetime. It is indicated that, in the recorded decay profiles, there are at least two components (τ_1 and τ_2), which are associated with the ET process from Eu^{2+} to Sm^{2+} in the crystal lattice. The determined emission lifetime values of Eu^{2+} ion as a function of Sm^{2+} content are presented in Table 1. Clearly, the average lifetime (τ) of Eu^{2+} decreases monotonically from 2.388 to 1.649 μs as the content of Sm^{2+} increases, which further confirms the efficient ET from Eu^{2+} to Sm^{2+} occurring in the Sm^{2+}–Eu^{2+} co-doped SrB_4O_7 system, in which the Eu^{2+} ions act as sensitizers and the Sm^{2+} ions act as activators. Additionally, the luminescence decay curves for all Stark sublevels of $^5D_0 \rightarrow {}^7F_0$, $^5D_0 \rightarrow {}^7F_1$ and $^5D_0 \rightarrow {}^7F_2$ transitions of Sm^{2+} ions, in the SrB_4O_7:0.01Sm^{2+},0.03Eu^{2+} system were measured and analyzed (see Fig. S6 in the ESI†). As shown in Table S6 in the ESI,† all the determined luminescence lifetimes for Sm^{2+} are similar, *i.e.* around 4 ms, because for all bands the emission occurs from the same excited state ($^5D_0$).

Conclusions

Incorporating Eu^{2+} ions into the crystal structure of the commonly used optical pressure sensor SrB_4O_7:Sm^{2+} (temperature-independent gauge), we have demonstrated a huge enhancement of about 60 times on the Sm^{2+} emission, induced by energy transfer processes from Eu^{2+} to Sm^{2+} in the co-doped material. The samples obtained exhibit color-tunable luminescence from orange-red to amaranth, and to warm white depending on the Sm^{2+} and Eu^{2+} concentrations in the matrix and the excitation wavelength. The most intense and extremely narrow (≈0.2 nm) 0–0 line of the Sm^{2+} (around 685 nm) in the best-enhanced sample (SrB_4O_7: 1 mol% Sm^{2+}, 3 mol% Eu^{2+}) was correlated with pressure and successfully calibrated up to about 58 GPa.

The emission line used for pressure sensing exhibit a large and linear red-shift under pressure, *i.e.* $d\lambda/dp \approx 0.29$ nm GPa^{-1}, a negligible temperature-induced band-shift and relatively low thermal quenching of luminescence. The energy transfer processes from Eu^{2+} to Sm^{2+} ions were confirmed by luminescence spectroscopy. Such favorable features can significantly extend the measurable pressure range, along with very high accuracy of pressure determination, even under high temperature conditions, and the material can be applied in white light emitting diode (LED) devices.

Conflicts of interest

The authors declare no competing financial interest.

Acknowledgements

This work was supported by the Polish National Science Centre, grant no. 2016/23/D/ST4/00296 and 2016/21/B/ST5/00110, The Ministerio de Economía y Competitividad (MINECO) under the Spanish National Program of Materials (MAT2016-75586-C4-4-P), The Agencia Canaria de Investigación, Innovación y Sociedad de la Información (ACIISI) (ProID2017010078), and grant no. POWR.03.02.00-00-I023/17 and POWR.03.02.00-00-i020/17 co-financed by the European Union through the European Social Fund under the Operational Program Knowledge Education Development, and by The EU-FEDER funds. M. R. is a recipient of the Bekker Programme scholarship supported by the Polish National Agency for Academic Exchange.

References

1 *An Introduction to High-Pressure Science and Technology*, ed. J. M. Recio, J. M. Menendez and A. Otero de la Roza, CRC Press, Boca Raton, 2016.
2 M. Runowski, S. Sobczak, J. Marciniak, I. Bukalska, S. Lis and A. Katrusiak, *Nanoscale*, 2019, **11**, 8718–8726.
3 F. Bai, K. Bian, X. Huang, Z. Wang and H. Fan, *Chem. Rev.*, 2019, **119**, 7673–7717.
4 M. Somayazulu, P. Dera, A. F. Goncharov, S. A. Gramsch, P. Liermann, W. Yang, Z. Liu, H. K. Mao and R. J. Hemley, *Nat. Chem.*, 2010, **2**, 50–53.
5 A. Cantaluppi, M. Buzzi, G. Jotzu, D. Nicoletti, M. Mitrano, D. Pontiroli, M. Riccò, A. Perucchi, P. Di Pietro and A. Cavalleri, *Nat. Phys.*, 2018, **14**, 837–841.
6 Z. Ma, Z. Liu, S. Lu, L. Wang, X. Feng, D. Yang, K. Wang, G. Xiao, L. Zhang, S. A. T. Redfern and B. Zou, *Nat. Commun.*, 2018, **9**, 4506.
7 W. Kim, M. S. Jung, S. Lee, Y. J. Choi, J. K. Kim, S. U. Chai, W. Kim, D. G. Choi, H. Ahn, J. H. Cho, D. Choi, H. Shin, D. Kim and J. H. Park, *Adv. Energy Mater.*, 2018, **8**, 1702369.
8 J. Song, G. Fabbris, W. Bi, D. Haskel and J. S. Schilling, *Phys. Rev. Lett.*, 2018, **121**, 037004.
9 L. Zhang, C. Liu, L. Wang, C. Liu, K. Wang and B. Zou, *Angew. Chem., Int. Ed.*, 2018, **57**, 11213–11217.
10 T. Yin, Y. Fang, W. K. Chong, K. T. Ming, S. Jiang, X. Li, J. L. Kuo, J. Fang, T. C. Sum, T. J. White, J. Yan and Z. X. Shen, *Adv. Mater.*, 2018, **30**, 1705017.
11 Th. Tröster, in *Handbook on the Physics and Chemistry of Rare Earths*, ed. K. A. Gschnidner, Jr., J.-C. G. Bünzli and V. K. Pecharsky, Elsevier, North-Holland, 2003, vol. 33, pp. 515–589.
12 P. M. Bell, H. K. Mao and K. Goettel, *Science*, 1984, **226**, 542–544.
13 J. A. Xu, H. K. Mao and P. M. Bell, *Science*, 1986, **232**, 1404–1406.
14 K. Syassen, *High Press. Res.*, 2008, **28**, 75–126.
15 G. J. Piermarini, S. Block, J. D. Barnett and R. A. Forman, *J. Appl. Phys.*, 1975, **46**, 2774–2780.
16 R. J. Angel, M. Bujak, J. Zhao, G. D. Gatta and S. D. Jacobsen, *J. Appl. Crystallogr.*, 2007, **40**, 26–32.
17 R. J. Angel, *Transformation Processes in Minerals*, De Gruyter, Mouton, 2019, vol. 39, pp. 85–104.
18 F. Datchi, R. LeToullec and P. Loubeyre, *J. Appl. Phys.*, 1997, **81**, 3333–3339.
19 C. Zhao, H. Li, Y. Wang, J. Jiang and Y. He, *High Press. Res.*, 2017, **37**, 18–27.
20 S. V. Rashchenko, A. Kurnosov, L. Dubrovinsky and K. D. Litasov, *J. Appl. Phys.*, 2015, **117**, 2–7.
21 Q. Jing, Q. Wu, L. Liu, J. Xu, Y. Bi, Y. Liu, H. Chen, S. Liu, Y. Zhang, L. Xiong, Y. Li and J. Liu, *J. Appl. Phys.*, 2013, **113**, 023507.
22 T. Zheng, L. Luo, P. Du, A. Deng and W. Li, *J. Eur. Ceram. Soc.*, 2018, **38**, 575–583.
23 Q. Dong, J. Cui, Y. Tian, F. Yang, H. Ming, F. Du, J. Peng and X. Ye, *J. Lumin.*, 2019, **212**, 146–153.
24 T. Zheng and L. Luo, *Ceram. Int.*, 2018, **44**, 12670–12675.
25 M. Runowski, *Handbook of Nanomaterials in Analytical Chemistry*, Elsevier, 2020, pp. 227–273.
26 M. Runowski, P. Woźny, S. Lis, V. Lavín and I. R. Martín, *Adv. Mater. Technol.*, 2020, 1901091.
27 H. Li, Q. Li and Z. Xu, *J. Mater. Chem. C*, 2019, **7**, 2880–2885.
28 H. Ji, L. Wang, M. S. Molokeev, N. Hirosaki, R. Xie, Z. Huang, Z. Xia, O. M. Ten Kate, L. Liu and V. V. Atuchin, *J. Mater. Chem. C*, 2016, **4**, 6855–6863.
29 V. V. Atuchin, A. S. Aleksandrovsky, O. D. Chimitova, T. A. Gavrilova, A. S. Krylov, M. S. Molokeev, A. S. Oreshonkov, B. G. Bazarov and J. G. Bazarova, *J. Phys. Chem. C*, 2014, **118**, 15404–15411.
30 Y. Shen and K. L. Bray, *Mater. Sci. Forum*, 1999, **315–317**, 243–248.
31 H. Fang, G. Qiu, J. Li and X. Wang, *J. Alloys Compd.*, 2018, **763**, 267–272.
32 W. J. Evans, *Coord. Chem. Rev.*, 2000, **206–207**, 263–283.
33 R. Shi, L. Ning, Y. Huang, Y. Tao, L. Zheng, Z. Li and H. Liang, *ACS Appl. Mater. Interfaces*, 2019, **11**, 9691–9695.
34 Z. Xia, Y. Zhang, M. S. Molokeev and V. V. Atuchin, *J. Phys. Chem. C*, 2013, **117**, 20847–20854.
35 Z. Wang, Z. Xia, M. S. Molokeev, V. V. Atuchin and Q. Liu, *Dalton Trans.*, 2014, **43**, 16800–16804.
36 H. Lai, J. Zhang, D. Hou, H. Guan and X. Ye, *Ceram. Int.*, 2018, **44**, 15072–15078.

37 L. Dong, L. Zhang, W. Lü, B. Shao, S. Zhao and H. You, *Dalton Trans.*, 2019, **48**, 3028–3037.
38 D. Liu, Y. Jin, Y. Lv, G. Ju, C. Wang, L. Chen, W. Luo and Y. Hu, *J. Am. Ceram. Soc.*, 2018, **101**, 5627–5639.
39 M. Shi, C. Zhu, M. Lu, X. Meng and M. Wei, *J. Am. Ceram. Soc.*, 2018, **101**, 5461–5468.
40 W. Wolszczak, K. W. Krämer and P. Dorenbos, *J. Lumin.*, 2020, **222**, 117101.
41 H. Dong, L. D. Sun and C. H. Yan, *Chem. Soc. Rev.*, 2015, **44**, 1608–1634.
42 S. Ye, F. Xiao, Y. X. Pan, Y. Y. Ma and Q. Y. Zhang, *Mater. Sci. Eng., R*, 2010, **71**, 1–34.
43 J. Xue, X. Wang, J. H. Jeong and X. Yan, *Phys. Chem. Chem. Phys.*, 2018, **20**, 11516–11541.
44 T. Zheng, M. Runowski, P. Woźny and S. Lis, *J. Alloys Compd.*, 2020, **822**, 1–9.
45 Z. Cao, X. Wei, L. Zhao, Y. Chen and M. Yin, *ACS Appl. Mater. Interfaces*, 2016, **8**, 34546–34551.
46 J. Sun, J. Zhu, X. Liu and H. Du, *J. Rare Earths*, 2012, **30**, 1084–1087.
47 P. Solarz, M. Karbowiak, M. Głowacki, M. Berkowski, R. Diduszko and W. Ryba-Romanowski, *J. Alloys Compd.*, 2016, **661**, 419–427.
48 S. Kobyakov, A. Kamińska, A. Suchocki, D. Galanciak and M. Malinowski, *Appl. Phys. Lett.*, 2006, **88**, 234102.
49 Q. Jing, Q. Wu, L. Liu, J. Xu, Y. Bi, Y. Liu, H. Chen, S. Liu, Y. Zhang, L. Xiong, Y. Li and J. Liu, *J. Appl. Phys.*, 2013, **113**, 023507.
50 M. Runowski, A. Shyichuk, A. Tymiński, T. Grzyb, V. Lavín and S. Lis, *ACS Appl. Mater. Interfaces*, 2018, **10**, 17269–17279.
51 M. Runowski, P. Woźny, V. Lavín and S. Lis, *Sens. Actuators, B*, 2018, **273**, 585–591.
52 P. Woźny, M. Runowski and S. Lis, *J. Lumin.*, 2019, **209**, 321–327.
53 M. Runowski, J. Marciniak, T. Grzyb, D. Przybylska, A. Shyichuk, B. Barszcz, A. Katrusiak and S. Lis, *Nanoscale*, 2017, **9**, 16030–16037.
54 X. Feng, D. C. Sayle, Z. L. Wang, M. S. Paras, B. Santora, A. C. Sutorik, T. X. T. Sayle, Y. Yang, Y. Ding, X. Wang and Y. Her, *Science*, 2006, **312**, 1504–1507.
55 X. Wang, Y. Wang, J. Yu, Y. Bu and X. Yan, *Opt. Express*, 2018, **26**, 21950.
56 D. Chen, Y. Yu, F. Huang, P. Huang, A. Yang and Y. Wang, *J. Am. Chem. Soc.*, 2010, **132**, 9976–9978.
57 R. Stefani, A. D. Maia, E. E. S. Teotonio, M. A. F. Monteiro, M. C. F. C. Felinto and H. F. Brito, *J. Solid State Chem.*, 2006, **179**, 1086–1092.
58 W. Liu, L. Liu, Y. Wang, L. Chen, J. A. McLeod, L. Yang, J. Zhao, Z. Liu, J. Diwu, Z. Chai, T. E. Albrecht-Schmitt, G. Liu and S. Wang, *Chem. – Eur. J.*, 2016, **22**, 11170–11175.
59 R. A. Hewes and M. V. Hoffman, *J. Lumin.*, 1971, **3**, 261–280.
60 M. V. Hoffman, *J. Electrochem. Soc.*, 1972, **119**, 905–909.
61 S. G. Jantz, F. Pielnhofer, L. van Wüllen, R. Weihrich, M. J. Schäfer and H. A. Höppe, *Chem. – Eur. J.*, 2018, **24**, 443–450.
62 R. Verstraete, H. F. Sijbom, J. J. Joos, K. Korthout, D. Poelman, C. Detavernier and P. F. Smet, *ACS Appl. Mater. Interfaces*, 2018, **10**, 18845–18856.
63 P. Cai, X. Wang and H. J. Seo, *Phys. Chem. Chem. Phys.*, 2018, **20**, 2028–2035.
64 M. Runowski, P. Woźny, N. Stopikowska, Q. Guo and S. Lis, *ACS Appl. Mater. Interfaces*, 2019, **11**, 4131–4138.
65 S. Stojadinović and R. Vasilić, *Mater. Lett.*, 2019, **234**, 9–12.
66 R. Reisfeld and C. K. Jørgensen, *Lasers and Excited States of Rare Earths*, 2012.
67 Q. Guo, Q. Wang, L. Jiang, L. Liao, H. Liu and L. Mei, *Phys. Chem. Chem. Phys.*, 2016, **18**, 15545–15554.
68 Q. Guo, C. Zhao, L. Liao, S. Lis, H. Liu, L. Mei and Z. Jiang, *J. Am. Ceram. Soc.*, 2017, **100**, 2221–2231.